INTELLIGENT MODELING AND PARAMETER OPTIMIZATION FOR MATERIAL REMOVAL RATE IN TRAVELING WIRE ELECTRO-CHEMICAL SPARK MACHINING PROCESS

Mohan Charan Panda
Professor
Mechanical Engineering Department
Gandhi Institute For Education & Technology, Baniatangi, Bhubaneswar – 752060, India

_____

Abstract : Manufacturing Engineers are facing new challenges during machining of electrically non-conducting or partially conducting materials such as glass, quartz, ceramics and composites. Traveling Wire Electrochemical Spark Machining (TW-ECSM), a largely unknown technology, has been applied successfully for cutting, these types of electrically non-conducting or partially conducting materials. However, very few theoretical works have been reported related to machining performance of TW-ECSM process. This paper reports, an intelligent approach for the modelling of TW–ECSM process using Finite Element Method (FEM) and Artificial Neural Network (ANN) in integrated manner. First, a 3-D finite element transient thermal model has been developed for the determination of MRR during TW–ECSM process. Using results from the FEM simulation, a three layer Back Propagation (BP) neural network process model was developed to predict MRR. The BP neural network process model was found to accurately predict TW–ECSM process response for chosen process conditions. Further, this paper also presents parameter optimization for MRR during TW–ECSM using Taguchi Method (TM). By analyzing, it is observed that spark on-time has more effect on MRR rather than supply voltage or current.

IndexTerms - Traveling Wire-Electro-Chemical Spark Machining (TW-ECSM), Material Removal Rate (MRR), Finite Element Method (FEM), Artificial Neural Network (ANN), Taguchi Method (TM).

_____

I. INTRODUCTION

Precision machining of electrically non-conducting or partially conducting engineering ceramics, composites, etc. is an urgent need of present industries. Machining of these materials by conventional methods is a serious problem yet to be resolved. Some of the advanced machining processes that can be used for machining these materials are Ultrasonic Machining (USM), Abrasive Jet Machining (AJM), Laser Beam Machining (LBM), and Electron Beam Machining (EBM). But these processes have their own limitations too. Electro Chemical Spark Machining (ECSM) process is an effective spark-based machining method suitable for machining of low machinability, high strength electrically conducting as well as non-conducting materials. ECSM is a hybrid process, which employs features of Electro Chemical Machining (ECM) and Electro Discharge Machining (EDM). However, ECSM can be applied to electrically non-conducting materials while the other two cannot be.

The ECSM process uses Electro-Chemical Discharge (ECD) phenomenon for generating heat for the purpose of removing work material by melting and vaporization. This was presented for the first time in 1968 by Kurafuji as "Electrochemical Discharge Drilling" for micro holes in glass (Kurafuli and Suda, 1968). Several other names of ECSM are used in literature by different researchers, such as "Electrochemical Arc Machining (ECAM)" by Kubota, "Electrochemical Discharge Machining (ECDM)" by Ghosh et al., and "Spark Assisted Chemical Engraving (SACE)" by Langen et al. (Wuthrich and Fascio, 2005). The diversity of names illustrates the complexity of the process. After almost 40 years of its first mention in literature, the basic mechanism of the process is not yet completely understood and is still a matter of research investigations. Various researchers have put forth explanations of ECD phenomenon based on their experimental studies (Basak and Ghosh, 1996, Jain et al, 1999, Kulkarni et al, 2002, Wuthrich and Bleuler, 2004, Yerokhin et al, 1999, Vogt, 1999, Fascio et al, 2004, Wuthrich et al, 2005) ECSM with ECD have been tried in many ways: Hole making using sinking tool electrode, Hole making using rotating tool electrode, Cutting using traveling wire tool electrode and Contour Milling (CM) using a simple shape tool electrode to produce 3-D cavity by adapting a movement strategy similar to conventional milling. Accordingly, they are called as Sinking-ECSM, Drilling-ECSM, TW-ECSM and CM–ECSM. Success in the application of Sinking and Drilling ECSM has stimulated interest in studying the prospects of TW-ECSM. In 1985 Tsuchiya et al. proposed TW-ECSM first time for cutting non-conducting materials such as glasses and ceramics and studied further on by Jain et al. and Peng et al. (Wuthrich and Fascio, 2005). TW-ECSM is capable to do slicing of large volume of material without the need for costly full form tool electrodes. Also, complex shapes in the workpiece can be cut by the use of numerically controlled movement of workpiece. In TW-ECSM configuration, a wire of diameter less than 1mm moves with speed less than few centimeters per minute through guides. TW-ECSM is a largely unknown technology for which scars literatures are available. Yet it has not been commercialized but still under laboratory study stage. McGeough et al. (1988) carried out experimental

studies on the effects of mode of electrolyte flushing, wire erosion, machining speed on metal removal rate during TW-ECAM. Their recommendation was to use coaxial mode of flushing for maintaining the machining action and its accuracy.

Jain et al. (1991) carried out experiments on their self developed setup of TW-ECSM for cutting Glass epoxy and Kevlar epoxy composites using NaOH electrolyte. They found that the wire wear rate and the over-cut follow a similar behavior as the machining rate but the wire wear rate is about two magnitudes smaller than the MRR. It was also found that there was increase in MRR at higher voltage along with the presence of thermal cracks, large HAZ and irregular machined surfaces. They also tried to study the effect of artificially introducing some bubbles into the process during machining and found that the MRR as well as the over-cut decreases slightly. Peng et al. (2004) verified that TW-ECDM can be applied for slicing meso-size non-conductive brittle materials of several millimeters thick. They have shown that pulsed dc power shows better spark stability and more spark energy than constant dc power. Nesarikar et al. (1994) carried out experimental study for the feasibility of TW-ECSM process for precision slicing of thick Kevlar-epoxy composite. They did comparison between the experimental and calculated values of MRR and average diametral overcut with the variations in electrolyte conductivity, applied voltage and specimen thickness.

Singh et al. (1996) attempted to explore the feasibility of using TW-ECSM process for machining of electrically partially conductive materials like PZT (lead zirconate titanate) and carbon fiber epoxy composites. They found that MRR increases with increase in supply voltage. MRR also increases with increase in concentration of the electrolyte up to around 20 wt %. Beyond this concentration it starts decreasing. They also observed that machined surface shows evidence of melting. Large cracks are sometimes observed when the machining is done at higher voltage. However, such cracking is not seen at lower voltage.

Basak and Ghosh (1997) developed a theoretical model for the electrochemical discharge machining process. The model has capability to predict the characteristics of the material removal rate for varying input parameters and gives similar trend of MRR with the experimental results. Jain et al. (1999) developed a 3-D unsteady heat transfer model for the determination of MRR, overcut and limited depth of cut during sinking-ECSM. In their model random number generation scheme to locate the spark over the workpiece has been used. They assumed the nature of the spark as prismatic column with square cross-section, which is far from real situation. Bhondwe et al. (2006) developed a FEM model for computation of MRR during sinking-ECSM. They applied the model to two types of materials, soda lime glass and alumina. Parametric study was also performed to study the effect of electrolyte concentration, duty factor and energy partition on MRR. Panda and Yadava (2009) developed a FEM model for computation of MRR during TW-ECSM. They applied the model to two types of materials, mild steel and glass. Parametric study was conducted by them to study the effect of energy partition, duty factor, spark radius, and ejection efficiency on MRR. They also performed computational experiments for the determination of energy partition and spark radius Based on the above literature survey, studied in depth, it has been observed that very few theoretical/numerical studies have been reported to date for the optimization of process parameters during TW–ECSM. The focus of the present work is on developing an intelligent process model for TW–ECSM process for accurate prediction of MRR. It primarily comprises development of two models. First one is the development of FEM model considering the thermo-physical characteristics of the TW–ECSM process and the second one is the development of an ANN model trained and tested by the data sets generated by FEM simulations. This approach of model development has a peculiar merit that it is based on the FEM model and not on experimental data collection, which is costly, time consuming and error prone. Further, parameter optimization for MRR during TW–ECSM process has also been carried out using Taguchi Method (TM). These optimum process parameters will help to improve the process productivity and finishing capability during TW–ECSM applications. "Figure 1" shows the overall methodology for the development of an integrated intelligent process model and optimization of process parameters during TW–ECSM process.

2. Numerical modeling of the TW–ECSM process

The configuration of a typical TW-ECSM setup is shown in "Fig. 2". In TW-ECSM the hydrogen gas bubbles are formed all along the circumference of the wire electrode. The coalescence of bubbles form a gas film around the wire electrode when the supply voltage reaches a critical value. This gas film isolates the wire electrode from the electrolyte. Electrical discharges in the form of sparks take place across gas film between tool and electrolyte and machining of material is possible if the workpiece material is kept in the vicinity of the sparking zone. The material removal in TW-ECSM is mainly caused by the melting and vaporization due to heat generated by the spark. It is considered as a thermal phenomenon (Wuthrich and Fascio, 2005). The equations used for modeling and simulation of TW-ECSM process include governing equation, boundary conditions and initial condition.

2.1 Assumptions

To make the analysis of TW-ECSM mathematically tractable numbers of simplifying assumptions are required to be made, which are written below:

i)   Workpiece material is homogeneous and isotropic. Although the materials used in real practice are not homogeneous in structure, to simplify the problem it is considered to be homogeneous throughout. Hence, the average values of thermal properties are used.

ii)   The thermal properties, viz. specific heat and thermal conductivity, of the workpiece material are treated as temperature independent.

iii)   Only a fraction of total spark energy is dissipated as heat into the workpiece. The rest of the heat is assumed to be distributed between the tool and the electrolyte. However, this study is restricted for the prediction of MRR from the workpiece material.

iv)   At a time only one spark is produced at the workpiece top surface (single Spark phenomenon) Kulkarni et al. (2002) and the duration of spark is same for all discharge.

v)   Shape of heat flux is assumed to be *Gaussian* distributed. From the experimental studies of Kulkarni et al. (2002) for single spark, the heat affected zone is circular and the crater is dome shaped. So reflecting the shape of crater, the nature of the heat flux can be approximated as *Gaussian*.

vi)   Since the study for the material removal is carried out for single spark, to calculate the material removal rate, the sparks occurring per unit time are assumed to be identical.

vii)   The energy density of a spark column during the discharge time t_{on} is assumed to be constant.

viii)   Ejection efficiency is assumed to be 100%. Also, there is no deposition of recast layer on the machined surface.

2.2 Governing Equation

The first step in estimation of MRR is to find the temperature distribution in the workpiece domain. The general 3-D heat diffusion equation within a homogenous and isotropic solid without heat generation in workpiece can be used. This can be written as Cengel, Y. A. (2004):

$$k\left[\frac{\partial^2 T}{\partial X^2}+\frac{\partial^2 T}{\partial Y^2}+\frac{\partial^2 T}{\partial Z^2}\right] = \rho C_p \frac{\partial T}{\partial t} \quad \text{in domain } ABCDEFGH \text{ (Fig.3)} \qquad (1)$$

Where, T is temperature, ρ is density, C_p is specific heat, k is thermal conductivity of the workpiece material, t is time and X, Y, Z are coordinate axes.

2.3 Initial and Boundary conditions

i)   At the start of the TW-ECSM process, the workpiece is immersed in the electrolyte and the temperature of the whole domain is assumed to be at room temperature (T_0) i.e., $T = T_0$ in the workpiece domain $ABCDEFGH$ at $t = 0$ (Fig.3).

(ii)   The boundaries B_3, B_5 and B_6 of the domain are considered as insulated boundaries (Fig.3). It is due to the fact that the temperature gradient across these boundaries (B_3, B_5 and B_6) compared to incoming heat flux boundary (B_q) is almost negligible

i.e., $\frac{\partial T}{\partial n} = 0$ on B_3, B_5 and B_6 for $t > 0$. $\qquad\qquad (2)$

Where, n is the outward normal to the boundary.

(iii)   On the top surface of the domain the area of B_q receives a total heat Q (from the spark) for a time period t_{on}. After that period, this area receives no heat as the spark moves to another location. Thus,

$$q_w = \frac{Q}{B_q} \quad \text{on area } B_q \text{ for } t \leq t_{on} \qquad (3)$$

$$= 0 \quad \text{for} \quad t > t_{on}$$

Where, q_w is the heat flux to the workpiece. The expression for q_w is given as:

$$q_w(r) = \frac{4.45 F_w UI}{\pi R^2}\exp\left\{-4.5\left(\frac{r}{R}\right)^2\right\} \qquad (4)$$

where, R is spark radius, r is the radial distance from the axis of the spark, U is supply voltage, I is current and F_w is energy partition.

No comprehensive method has so far been proposed to calculate the value of F_w during TW-ECSM process. Jain et al. (1999) assumed this value as 5%. Therefore, in the present work F_w is taken as 5%. Basak and Ghosh (1997) took spark diameter $2a = 10^{-6} I_b$, where $2a$ is spark diameter in meters and I_b is the current in amperes at the instant of the circuit opening. But they assumed that spark channel is cylindrical in shape. Also Jain et al.(1999) assumed prismatic nature of spark with square cross section, which is far from real situation. Kulkarni et al. (2002) gave the crater diameter for different workpiece materials as 300 μm based on their experiments. Therefore, in the present work, the spark radius is taken as 150 μm.

During on-time the remaining area ($B_1 - B_q$) on the top surface of the domain (Fig. 3) losses heat due to convection to the surrounding electrolyte. The area ($B_1 - B_q$) will however depend on the location of the discharge. Also, during off time the

whole top surface B_1 will be the convective boundary. The boundaries B_2 and B_4 are also considered as convective boundaries as it will dissipate heat throughout the computational time, irrespective of on or off time. Hence, we can write,

$$q_c = h(T - T_O) \qquad \text{on } B_1 - B_q, B_2, \text{ and } B_4 \text{ for } t > 0 \qquad (5)$$

Where, h is convective heat transfer coefficient of the electrolyte ($W/m^2 - K$) in which workpiece is completely dipped.

2.4 Finite Element Formulation

In the present analysis, the Galerkin's weighted residual method Reddy (2005) has been applied to obtain the temperature distribution within the computational domain (Fig. 3b) due to heat flux of single spark. The following elemental equations are obtained when Galerkin's approach is applied to TW-ECSM process [Eqs. 1-5].

$$[C]^e \left\{ \overset{\bullet}{T} \right\}^e + [K]^e \{T\}^e + [K]^b \{T\}^b = \{f_c\}^b + \{f_q\}^b \qquad (6)$$

where,

$$\left.\begin{aligned}
[C]^e &= \int_{D^e} \rho C_p \{N\}^e \{N\}^{eT} \, dD^e \\
[K]^e &= \int_{D^e} k [B]^{eT} [B]^e \, dD^e \\
[K]^b &= \int_{B_h} h \{N\}^b \{N\}^{bT} \, dB_h \\
\{f_c\}^b &= \int_{B_h} T_0 h \{N\}^b \, dB_h \\
\{f_q\}^b &= \int_{B_q} \{N\}^b q_w \, dB_q
\end{aligned}\right\} \qquad (7)$$

Here, $[C]^e$ is the elemental capacitance matrix, $[K]^e$ is the elemental conductivity matrix, $[K]^b$ is the boundary elemental conductivity matrix, $\{f_c\}^b$ is the boundary element convection vector, $\{f_q\}^b$ is the boundary element heat flux vector, $\{N\}^e$ is the interpolation functions vector for a typical area element, $\{N\}^b$ is the interpolation functions vector for a boundary element, $[B]^e$ is the matrix of derivatives of nodal interpolation functions for typical area element, B_h is the convective boundary and B_q is boundary of input heat flux. The Gauss quadrature technique is used to evaluate elemental matrices and vectors. When elemental quantities of Equation (7) are assembled, the following differential equations are obtained.

$$[GC] \left\{ \overset{\bullet}{T} \right\} + [GK] \{T\} = \{GF\} \qquad (8)$$

Where, $[GC]$ is the global capacitance matrix, $[GK]$ is the global stiffness matrix, $\{GF\}$ is the global heat flux vector, $\{T\}$ is global temperature vector and $\left\{ \overset{\bullet}{T} \right\}$ is time derivative of $\{T\}$. Equation (8) is converted into algebraic equations after application of implicit Finite Difference Method (FDM). Here, the solution marches in time, in steps of Δt until the desired final time is reached. In the present model, Δt is divided into two-time steps Δt_1 and Δt_2. Δt_1 and Δt_2 are pulse on time and off time of the spark, respectively.

2.5 Modelling for material removal rate (MRR)

For calculation of MRR from the workpiece during TW-ECSM it is assumed that the discharge occurs only along the axis of the wire and only one discharge occurs at any instant. Also, it is considered that no consecutive sparks occur at the same location. The cathode wire is considered to move along the X-axis at Z=0.6mm on top surface (X-Z plane) of the workpiece (Fig. 3). The velocity of the wire (V_w) is taken as 2m/min [11]. Total distance traveled by the wire across the workpiece is 0.6mm (from X=0 to X=0.6mm). On-time and off-time of the spark is taken as 500µs and 100µs respectively. So, total pulse duration is 600µs. Hence, time required to travel across the workpiece width (0.6mm) is calculated as 18000µs. During this duration 30 numbers of sparks are possible. This requires a discritized domain of atleast 30 locations on which sparking can occur. It is assumed that the sparks occurring at a place do not overlap and the sparks should fall completely on the top surface of the domain as shown in "Fig. 4". Hence, for 30 spark locations a domain having nodes more than 4500 is required. Present computing machine available is not capable to perform calculations with array size more than 4500×4500. Due to this limitation, wire travel distance across the workpiece is not considered for 0.6mm.Instead MRR is calculated based on only computational time of 1200µs when wire travels a distance of 0.04mm over the workpiece. During this computational time two sparks are possible. This way wire velocity has been incorporated in the calculation of MRR.

The location of the first spark is assumed at X=0.15mm, Z=0.6mm on top surface (X-Z plane, Y=0.6mm) as shown in "Fig. 4". The nodal values of input heat flux for the boundary elements on the top surface of workpiece is the function of radius from the center of axis of the spark as given by Equation (4). Using the global coordinates of each node of the boundary element, the distance from the axis of the spark is calculated. The distance of each node of a boundary element is compared with the radius of spark. If distance of atleast one node of a boundary element is less than the radius of the spark or if the distance of atleast two nodes of a boundary element are equal to distance of radius of spark, the element is taken as incoming heat flux boundary, else the element is taken as convective boundary element. This logic is incorporated in the developed software. So, when the location and radius of the spark is specified, the software can locate the incoming heat flux boundary elements and convective boundary elements on the top surface of the workpiece.

After the on-time of the first spark, an off-time of 100µs is considered. During this period the whole top surface DHGC (Fig. 3) will be considered as convective boundary. The second spark is assumed at X=0.45mm, Z=0.6mm on X-Z plane at Y=0.6mm as shown in "Fig. 4". The temperature distribution in the workpiece domain at the end of the first pulse duration is used as the initial temperature for the calculation of nodal temperature for the second pulse duration.

Contour plots of temperature at the top surface of the workpiece after the first and second spark at X=0.15mm and X=0.45mm are shown in "Fig. 5". "Figure 5" (a) and "Figure 5 (b)" show the contour plots after first and second spark respectively. Isotherms are also plotted at different X-Y sections (depth direction) of the domain for different voltage and machining current. The isotherms in X-Y plane at Z=0.6mm for 20V and 25A input power are shown in Fig. 6. Isotherms in X-Y plane after the first and second spark are shown in "Fig. 6 (a)" and "Fig. 6 (b)" respectively. The volume of the material melted is computed by generating the isotherms for the temperature equal to and above the melting temperature (T_m) of the workpiece material. This is done by interpolating the nodal temperatures on the top surface as well as in the depth direction of the workpiece. The isotherms in "Fig. 5" and "Fig. 6" show the crater formed in the workpiece material. The volume of the crater formed is calculated by assuming its shape to be of hemi-ellipsoid. The volume V of a hemi-ellipsoid is given by, $V = \frac{2}{3} \times \pi \times a \times b \times c$ where, a, b and c are the half axes of the ellipsoid Jain et al (1999).

Initially the MS workpiece is at the room temperature (20°C). When the workpiece is subjected to the first spark the temperature of the workpiece increases. At the end of the first spark the volume of material having temperature more than the melting temperature (1150°C) of MS are removed from the workpiece. The remaining workpiece material will be at a higher temperature than the room temperature. These temperatures are stored to use as initial temperature of the workpiece for calculation of nodal temperature in the workpiece due to second spark. The volume after the first spark and the volume removed by the second spark are added to get the total volume of material removed due to two sparks, i.e., total duration of two sparks are 2×600 µs. MRR is then calculated using Equation (9).

$$MRR = \frac{(V_1 + V_2) \times 60}{(t_{p1} + t_{p2}) \times 10^{-6}} \ mm^3/\min$$

V_1 = Volume of material removed after first spark (mm^3)

V_2 = Volume of material removed after second spark (mm^3)

t_{p1} = First pulse duration (µs)

t_{p2} = Second pulse duration (µs)

since t_{p1} is taken same as t_{p2} ($t_{p1} = t_{p2}$), hence

$$MRR = \frac{(V_1 + V_2) \times 60}{2 \times t_{p1} \times 10^{-6}} \ mm^3/\min$$

(9)

2.6 Comparison of MRR

McGeough et al. (1988) experimentally measured MRR from MS workpiece during TW-ECSM. In their experiment a copper wire of 0.25 mm diameter was used as cathode electrode moving with a velocity of 2 m/min. The thickness of MS workpiece was 12 mm. The NaNO3 electrolyte, with a 200 g/l solution at 20˚C was used. Each experiment was lasted for about 6 to 12 min, during which current and voltage were recorded on a coulomb counter and oscilloscope respectively.

The above-mentioned problem is solved using present model for determination of MRR from MS workpiece during TW-ECSM. The wokpiece material and cutting conditions used are taken same as used in the literature McGeough et al. (1988). The material properties of mild steel are taken from Nayar (2002). The cutting conditions and the material properties of mild steel are given in Table 1 and Table 2 respectively. The domain size has been changed from 12mm×6mm×6mm to 1.2mm×0.6mm×0.6mm because of computational limitations of our computing system. The workpiece domain is discretized into eight noded hexahedral elements. Convergence conditions were carried out by increasing the number of elements in the mesh. The simulation showed that the nodal temperature of workpiece domain obtained were essentially unchanged, when the mesh size is in excess of 1024 elements. The mesh of 1024 elements is thus found to be adequate for convergence. Hence the mesh consisting of 1024 number of square elements each of length 0.075 mm and total 1377 nodes are used for further analysis. The nodal temperature distribution of the workpiece domain is found using computer with Pentium 4 processor.

MRR is calculated for different supply voltage and machining current. MRR calculated using present FEM based model is compared with experimental values obtained by McGeough et al. (1988). The results obtained using present model shows (Fig. 7) similar pattern as given in literature McGeough et al. (1988). MRR calculated using present FEM based model increases with increase in voltage. MRR also increases with the increase in feed rate. Calculated MRR at feed rate of 10 mm²/min and supply voltage of 15V using present FEM based model is found as 38.58mm³/min whereas the experimental value of MRR for the same input conditions is 30mm³/min. Further, when the feed rate is taken 10mm²/min and supply voltage 20V the MRR calculated using present FEM based model is found 65.33mm³/min whereas experimental value is 40mm³/min.

Hence, it is observed that MRR calculated using present model is greater than experimental values. This may be due to the value considered for ejection efficiency during TW-ECSM process. In the present model the ejection efficiency is assumed to be 100% (it is assumed that all the material, which is melted, is removed). In real situation, some part of the molten material is not completely removed but it adheres back (resolidify) to the parent material because of the quenching effect caused by liquid electrolyte. This plays a dominant role, as the ejection efficiency in TW-ECSM is very low. It may be as low as 10% or even lower than that Jain et al. (1991). Further there is no exact data available regarding energy partition and spark radius for the combination of MS workpiece, NaNO₃ electrolyte and Cu traveling wire. Also, shape of the crater formed is assumed as hemi-ellipsoid and approximations are done in the calculation of volume during interpolation of co-ordinates of isotherms. Above described reasons are responsible for getting different values of computational and experimental results.

Parametric study was conducted considering Glass as workpiece material and using the model developed for MRR. The material properties of Glass are given in Table 3. From the parametric study conducted, it has been found that MRR during TW–ECSM process is influenced by different input process parameters. It is observed that a complex, non linear relationship exist between these process parameters with MRR. In the absence of a good process model, it is quite difficult to select the optimum process parameters. Hence the results obtained from the present FEM model have further been used for developing an intelligent model for simulation and optimization of TW–ECSM process for specific application. Neural networks are known to have excellent function mapping capabilities even from incomplete and noisy data Hassoun (2007). It is therefore thought that an appropriate ANN-based comprehensive TW–ECSM process model can be developed using the simulation results of FEM-based model.

3. Intelligent modeling of the TW–ECSM process

Artificial Neural Networks are developed to model the way in which the human brain performs a particular task, or processes information. ANNs are parallel computational models comprised of densely interconnected adaptive processing units and have gained prominence recently among researchers of non-linear systems. As the name implies, these networks are computer models of the processes and mechanisms that constitute biological nerve systems. ANNs can be used to model complex relationships between inputs and outputs or to find patterns in data. In essence, a neural network can be viewed as function approximater for approximating outputs for given set of input conditions with proper training. ANNs have the ability to learn from their environment and adapt to it in an interactive manner similar to the biological neurons Zurada (2006). A very important feature of these networks is their adaptive nature, where 'learning by example' replaces 'programming' in solving the problems Karunakar and Datta (2008) This feature makes such computational models very useful in application domain where one has little or an incomplete understanding of the problem to be solved.

3.1 Back propagation artificial neural network modeling of TW–ECSM process

The present work was aimed at establishment of correlation between input process parameters such as supply voltage, current and spark on-time with process response MRR using suitable ANN algorithm. There are several algorithms in ANN and the one that has been used in the present study is the back-propagation (BP) training algorithm. In the back-propagation network, initially the weights are initialized randomly. Consequently, the outputs are calculated based on these weights. Outputs so calculated are compared with the actual or desired outputs by the network and the error is transmitted to the previous layer, which results in correction of the weights. The training iteration process may be terminated either by a convergence limit or simply by limiting the total number of iterations. The steps of the ANN calculation during training using back propagation algorithm are as follows.

1st step: Specify a set of desired input/output patterns for the NN.

2nd step: Synaptic weights of the network are initialized to small random values.

3rd step: An input pattern from the set of desired input/output patterns is presented and the network responses are calculated.

4th step: The desired network responses are compared with the actual output of the network and the mean square error (MSE) is computed.

5th step: The weights preceding each output node are updated according to the following update formula Jain and Jain (2000).

$$\Delta w_{ij}(n) = \alpha w_{ij}(n-1) + \eta \delta_j y_i(n) \qquad (10)$$

where, η is a constant called learning rate, δ is the local error gradient of the network, α is usually a positive number called momentum factor, y_i the output of the ith unit, n is the number of training pattern presented to the network, and w_{ij} represents the weight connecting the ith neuron of the input vector and the jth neuron of the output vector.

6th step: The cycle (step 3 to step5) is repeated until the calculated outputs have   converged sufficiently close to the desired outputs or an iteration limit has been reached.

3.1.1 Network training and testing data

In this work as discussed in section 2, thermophysical analysis of single-spark TW–ECSM process using FEM has been carried out and same is used for the determination of MRR. Considering three input process parameters (supply voltage, current and spark on-time) at five different levels (Table 4) a total of 125 (5^3) numerical experiments have been carried out to calculate the values of MRR. These data sets were divided into a training set and a testing set for ANN simulation. Out of the total available 125 data sets, for selecting the testing data sets Taguchi's L_{25} orthogonal array (Table 5) was used and remaining 100 data sets were used for training the network. In order to increase accuracy and speed of the network the input and output data were normalized. After normalization input and output data set lies in between 0.1 and 0.9. The training and testing datasets were normalized using the following equation.

$$x_n = \frac{0.8(x - x_{min})}{x_{max} - x_{min}} + 0.1 \qquad (11)$$

where x_n is the normalized value of variable x, x_{max} and x_{min} are maximum and minimum value of x in total data sets.

3.1.2 Training and testing of neural network

By training the neural network, the architecture of the network has been decided; i.e. the number of hidden layers and number of neurons in each layer. As there are three inputs and one output in the present problem, the number of neurons in the input and output layer has to set to three and one, respectively. As the number of hidden layers in the network increases, the complexity increases. Further, according to Fausett (1994) the back-propagation architecture with one hidden layer is enough for the majority of applications. Hence, in the present case only one hidden layer has been considered. No standard guidelines are available for selecting the number of neurons in the hidden layer. A trial and error method was employed to select the number of neurons in the hidden layer in which the mean prediction error (MPE) obtained is minimum. Error value is the numerical difference between the FEM result of the output performance parameter and the value predicted by the trained network. The absolute prediction error (APE) is defined as:

$$APE(\%) = \left| \frac{\text{FEM result - ANN predicted result}}{\text{FEM result}} \right| \times 100 \qquad (12)$$

Then, the MPE of the testing datasets for output performance parameter (MRR) was calculated.

$$MPE(\%) = \frac{\sum\limits_{i=1}^{t} APE}{t}$$

Where t = 25 is the number of datasets used for testing.

This MPE was further used for selecting the optimal network configuration.   Extensive numerical experimentations were carried out using self developed ANN based MATLAB code to select the optimal network architecture. The following parameters were used to successfully train the network.

Learning rate (η) = 0.5, momentum factor (α) = 0.1, maximum number of epochs = 10,000, tolerance for MSE = 0.01.

Figure 8 shows the ANN architecture proposed for the present problem. It considers supply voltage, current and spark on-time as input parameters to predict MRR. In this architecture, a single hidden layer was taken and the number of hidden neurons (N) was varied from three to eighteen. BP neural network simulations were carried out. "Figure 9" shows the variation of MPE with the number of neurons in the hidden layer. The BP neural network with seven neurons gave minimum MPE. Fig. 10 depicts the variation of MSE with number of epochs during the training of the BP neural network with seven hidden neurons.

Table 6 shows the absolute prediction error of the $3 - N - 1$ BP neural network architecture with 7 hidden neurons for the single output performance parameter. Actual and predicted values from the network for MRR have been shown in "Fig. 11". The results show acceptable prediction accuracy of the BP neural network based process model developed for the prediction of MRR with prediction error within the range of $0.769 - 19.079$ % with the average accuracy of 3.1%. It is also observed that a total of 88% of the total testing datasets lie within 4% of error bound. Hence, the developed ANN based process model can be used to select optimum process conditions to improve TW–ECSM process productivity and finishing capability.

4. Parameter optimization using Taguchi method

Taguchi method is a widely accepted method of design of experiments (DOE). The objective of Taguchi approach is to determine the optimum setting of process parameters or control factors, thereby making the process insensitive to the sources of variations due to uncontrollable or noise factors. In Taguchi Methodology, signal-to-noise (S/N) ratio is used to represent quality characteristic for the observed trial data. Here, the 'signal' represents the desirable value and the 'noise' represents the undesirable value and signal to noise ratio expresses the scatter around the desired value. The larger the ratio, the smaller will be the scatter Phadke (1989). Depending upon the objective function of the quality characteristic there can be various types of S/N ratios. The S/N ratio is mathematically represented as:

$$S/N = -10\log_{10}(\text{MSD}) \tag{13}$$

where, MSD represents the Mean Square Deviation of observed trial data from the desired value and commonly termed as quality loss function. The MSD is calculated by using different expressions depending upon whether the problem is of the lower is better (LB), the higher is better (HB), or the nominal is best (NB) type. The quality loss function or MSD for these three types of characteristics can be computed as:

$$\text{For LB-type,} \quad \text{MSD} = \left[\frac{1}{n}\sum_{i=1}^{n} y_i^2\right] \tag{14}$$

$$\text{For HB-type,} \quad \text{MSD} = \left[\frac{1}{n}\sum_{i=1}^{n} \frac{1}{y_i^2}\right] \tag{15}$$

$$\text{For NB-type,} \quad \text{MSD} = \left[\frac{1}{n}\sum_{i=n}^{n} (y_i - M)^2\right] \tag{16}$$

here, y_i is the observed data (or quality characteristics) at the ith trial, M is the Target value and n is the number of trials.

The aim is always kept to maximise the S/N ratio whatever may be the nature of quality characteristics. The average value of all S/N ratios when a parameter is at same distinct level is used to describe the effect of a parameter or factor on quality characteristics at that level. A parameter level corresponding to the maximum average S/N ratio is called the optimum level for that parameter. A better feel for the relative effect of the different parameters can be obtained by the decomposition of the variance, which is commonly called analysis of variance (ANOVA). It is a computational technique to estimate quantitatively the relative contribution that each control factor or parameter makes on the overall measured response. A confirmation test is performed by conducting a test using a specific combination of the factors and levels previously evaluated. The purpose of the confirmation test is to validate the conclusions drawn during the analysis. The predicted value of mean at optimum parameter level (m_{opt}) is calculated by using following equation, Rose (2005):

$$m_{\text{opt}} = m + \sum_{i=1}^{cf} (m_{mi} - m) \tag{17}$$

where m is the mean of all trials, cf is the significant number of control factors, and m_{mi} is the average mean for i^{th} control factor corresponding to optimum parameter level. The experimenter would prefer to have a range of values within which the true average would be expected to fall with some confidence. The confidence interval is a maximum and minimum value between which the true average should fall at some stated percentage of confidence. The confidence interval of confirmation test was calculated by using following equation [28]:

$$CI_{CT} = \sqrt{F_a(1, f_e)V_e \left[\frac{1}{n_{eff}} + \frac{1}{u}\right]} \tag{18}$$

where $F_a(1, f_e)$ is the F ratio at a confidence level of $1 - \alpha$ against dof 1 and error dof f_e, V_e is the error variance and n_{eff} is the effective number of replications. The effective number of replications can be calculated as Rose (2005):

$$n_{eff} = \frac{N}{1 + \left[\text{Total dof associated in the estimate of mean}(m_{opt})\right]}$$

where N is the total number of trials, u is the sample size of the confirmation test. The predicted optimum range can be taken as Rose (2005):

$$m_{opt} - CI_{CT} < m_{opt} < m_{opt} + CI_{CT}$$

4.1 Analysis and discussion of results

For the present problem, higher value of MRR as the target value is desirable. The S/N ratio for MRR is calculated using the ANN predicted output parameter values given in Table 5. The S/N ratio value corresponding to each trial is given in Table 7. The mean response refers to the average value of the performance characteristic for each parameter at five levels. The average values of the performance characteristic (raw data) for each parameter (supply voltage, current and spark on-time) at five levels are calculated and given in Table 8. The maximum average factor effect of parameters for maximum MRR is obtained at level 5 (60V) of supply voltage, level 5 (50A) of current and level 5 (0.0009s) of spark on-time. The effect of an input parameter at particular level is also computed by taking the average of all S/N ratio values at the same level. The effect of various factors when they are changed from the lower level to higher levels for response MRR is shown in Table 9. Also, the graphical representations of factors effect on MRR based on average S/N ratio values is shown in "Fig. 12". It is always required to maximise the S/N ratio whatever may be the nature of quality characteristics. Hence, it is observed from the response graph "Fig. 12" that the optimum parameter level combinations for maximum value of MRR are $A_5 B_5 C_5$.

In order to study the significance of the process parameters towards MRR the analysis of variance (ANOVA) is performed. The results of ANOVA based on raw data are given in Table 10. The ANOVA is also performed on S/N ratio values. The results of ANOVA based on S/N ratio values are given in Table 11. The contribution of factors in increasing order for MRR is supply voltage (14.45%), current (22.15%) and spark on-time (56.35%).

The optimum values of MRR can be predicted at the selected levels of significant parameters. The significant process parameters and their optimum levels have already been selected. The estimated mean (m_{opt}) of the response characteristic (MRR) can be computed by using equation 17. The value of m_{opt} has been calculated as 763.7198. The confidence interval of confirmation trial (CI_{CT}) for 95% confidence level has been calculated by using equation 18. For finding CI_{CT} for 95% confidence level of predicted mean for MRR the values of $F_{0.05}$ (1, 12), N, R, V_e and the total dof associated in the estimation of mean are taken as 4.75, 25, 1, 413.33 and 12 respectively. The calculated value of CI_{CT} has been found as 53.9046. So, for 95% confidence level the predicted mean will lie in the interval: 709.8152< MRR < 817.6244.

Confirmation test is performed by conducting computational experiment with optimal settings of the factors and levels previously evaluated (Table 9). The results of confirmation test is shown in Table 12 which shows that the value of MRR at this optimum level of parameters setting is 812.751mm^3/min against the initial parameter setting of 74.0095mm^3/min. It has been found from the confirmation test that the computed MRR at the optimum level of parameter setting are within the confidence interval of the predicted optimal values of MRR at 95% confidence level.

5. Conclusions

The present work, parameter optimization for MRR during TW–ECSM using Taguchi Method (TM), based on ANN predicted process responses in which FEM simulation results were used for training and testing represents a new approach of optimization. Following conclusions have been derived from the present analysis.

1. The trend of variation of computed MRR with feed rate has been found similar to that observed experimentally. The computed MRR values are found higher than those obtained experimentally because of 100% ejection efficiency consideration.
2. Extensive numerical simulations were carried out to select the optimal BP neural network architecture by varying the number of neurons in the hidden layer. The 3 – 7 – 1 optimal network architecture was found to give good average prediction accuracy for MRR as 3.1%.
3. The optimum value of control factors for maximum MRR is: supply voltage – 60V, current – 50A and spark on-time – 0.0009s.
4. The contribution of factors in increasing order for MRR is supply voltage (14.45%), current (22.15%) and spark on-time (56.35%).
5. Improvement in MRR by 998% has been found while machining at their optimum parameter setting against their initial parameter setting.
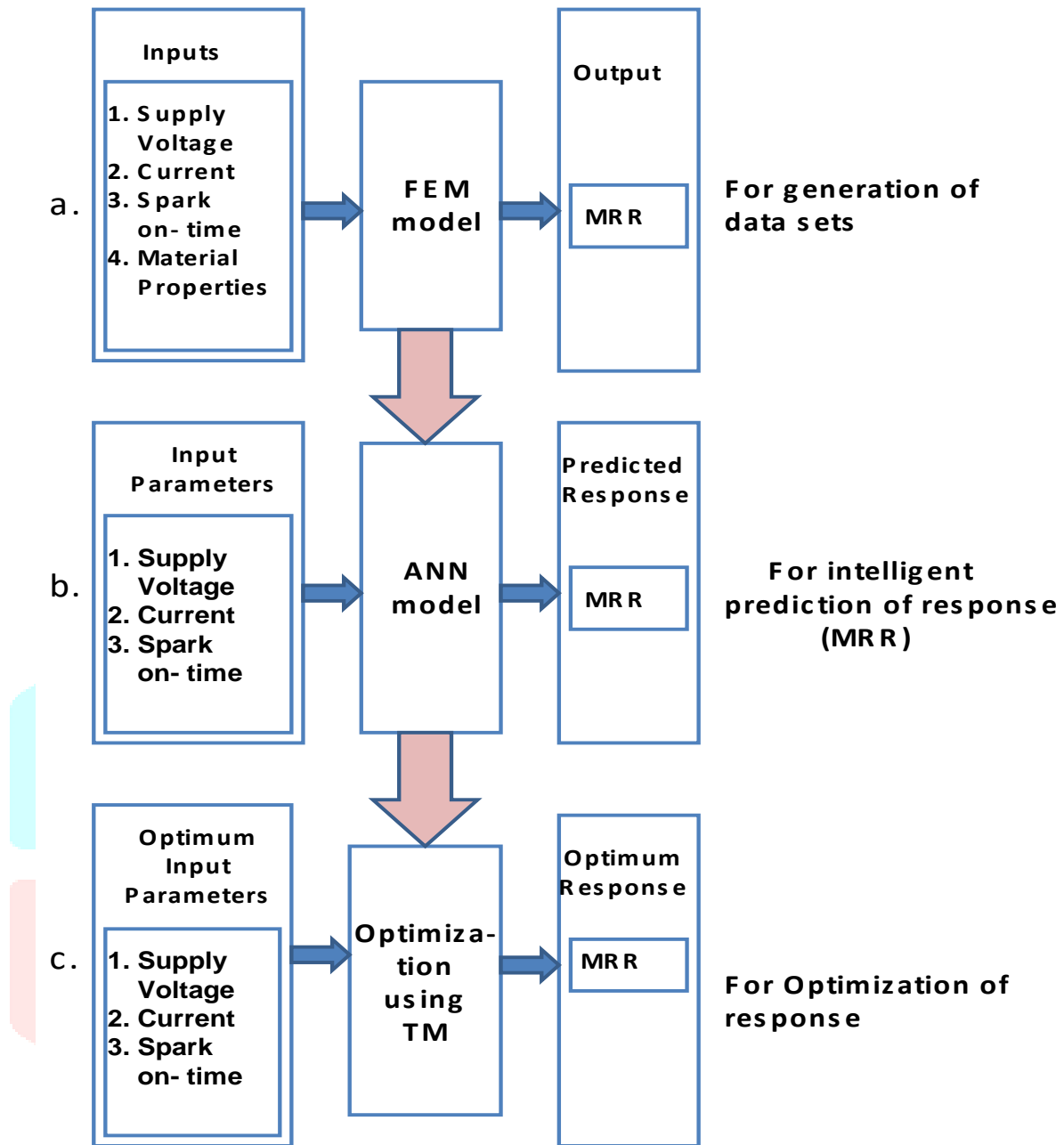
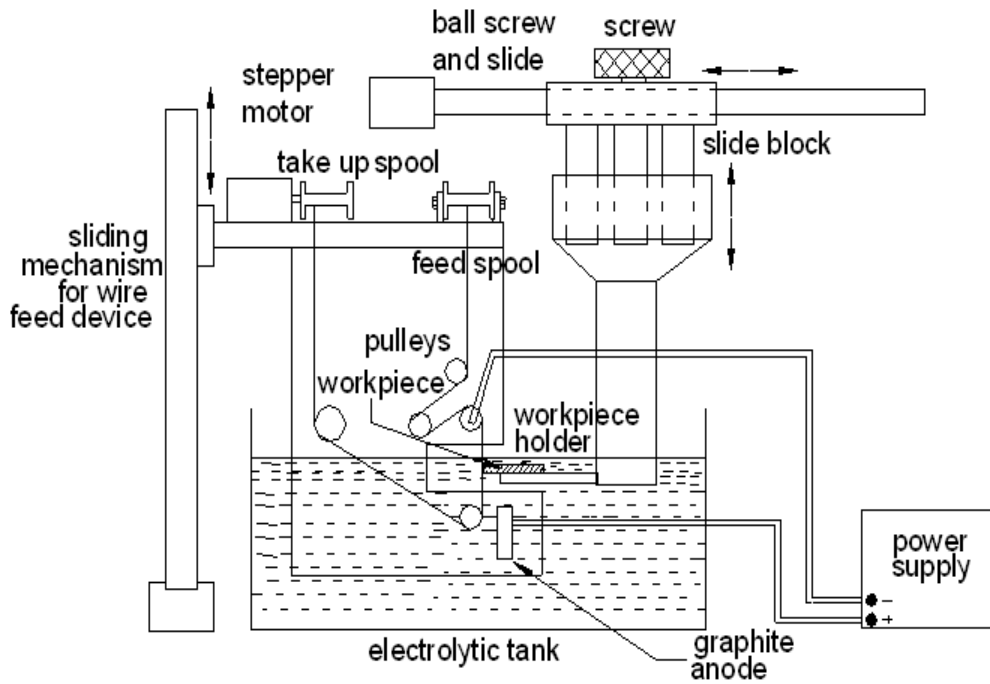Fig.1 Integrated process model development for TW–ECSM process and its optimization
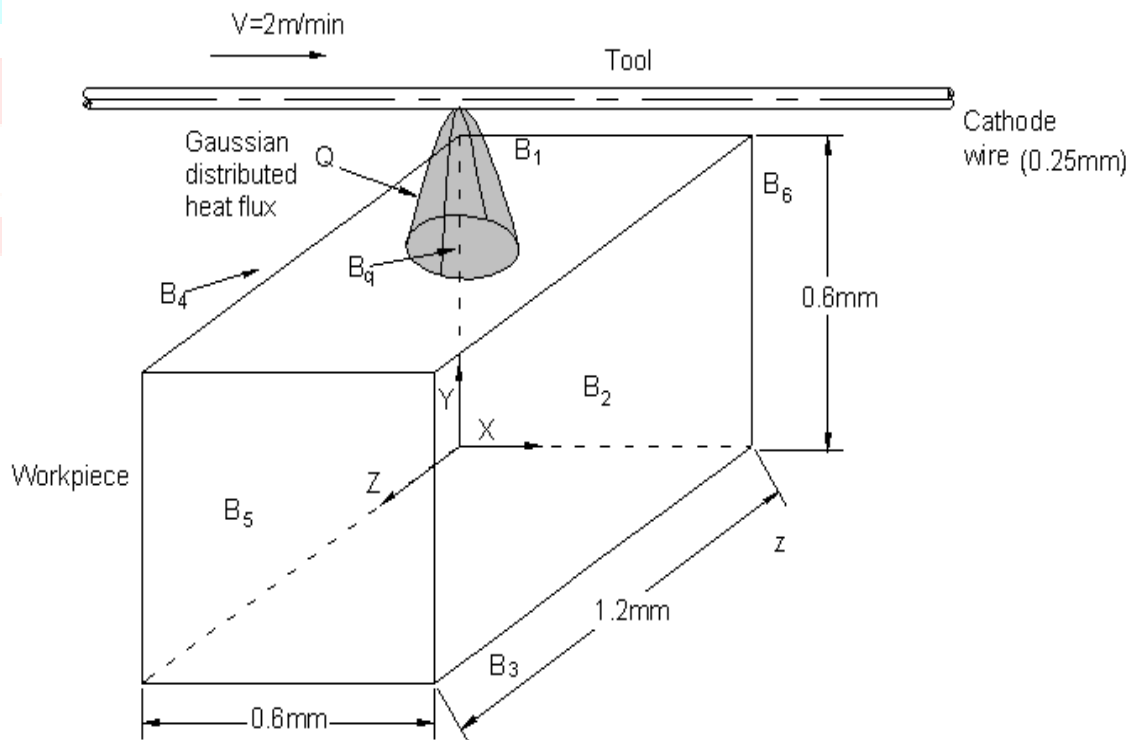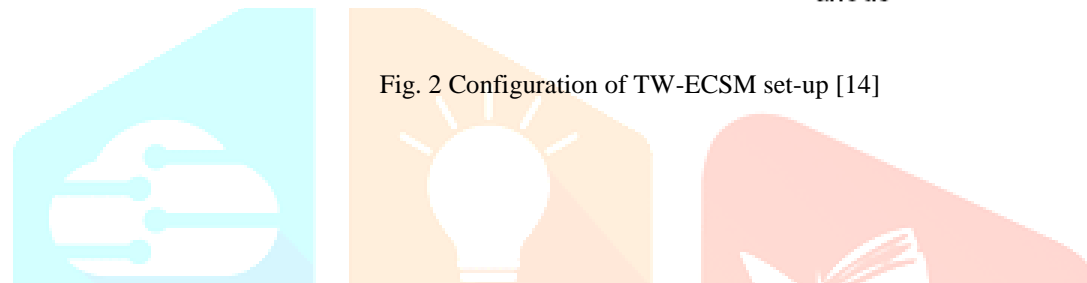
Fig. 2 Configuration of TW-ECSM set-up [14]
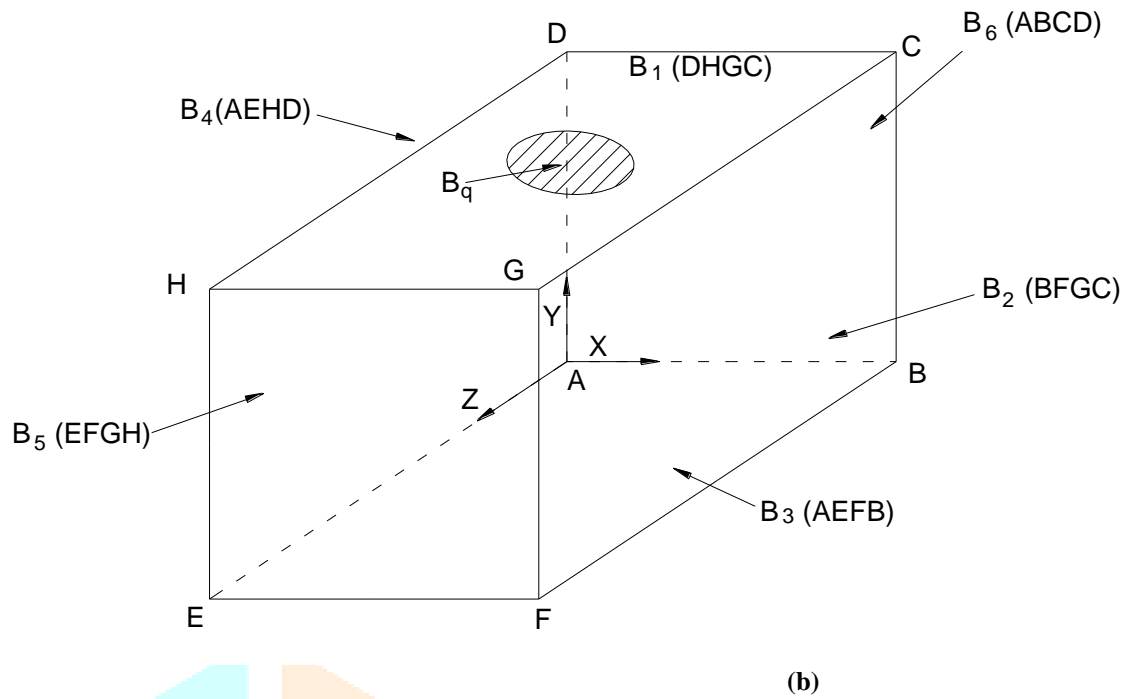

(a)

(b)

FIG. 3 (A) GEOMETRICAL MODEL   FOR TW-ECSM (B) COMPUTATIONAL DOMAIN WITH BOUNDARY CONDITIONS
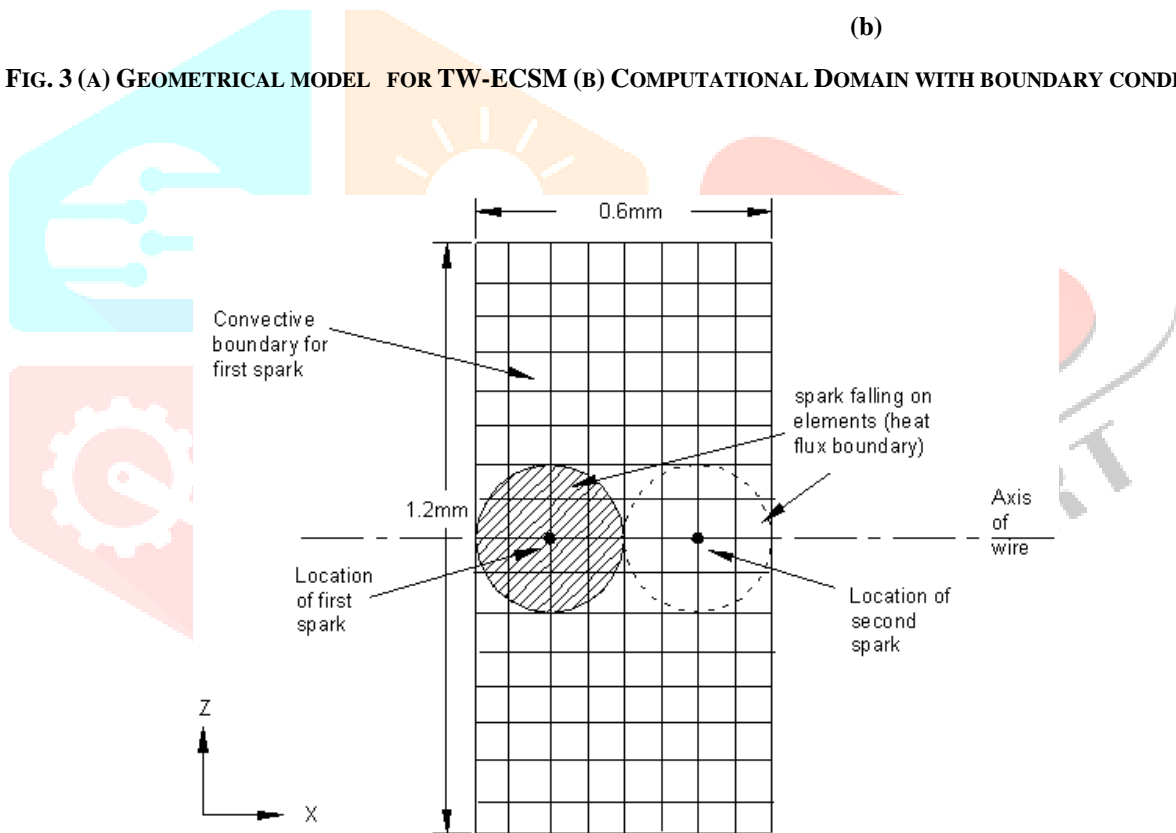

Fig. 4 Location of two sparks on X-Z plane at Y=0.6mm

Fig. 5 Contour plots on X-Z plane at Y=0.6mm for 20V and 25A input power supply (a) after first spark at location X=0.15mm, Z=0.6mm (b) after second spark at location X=0.45mm, Z=0.6mm
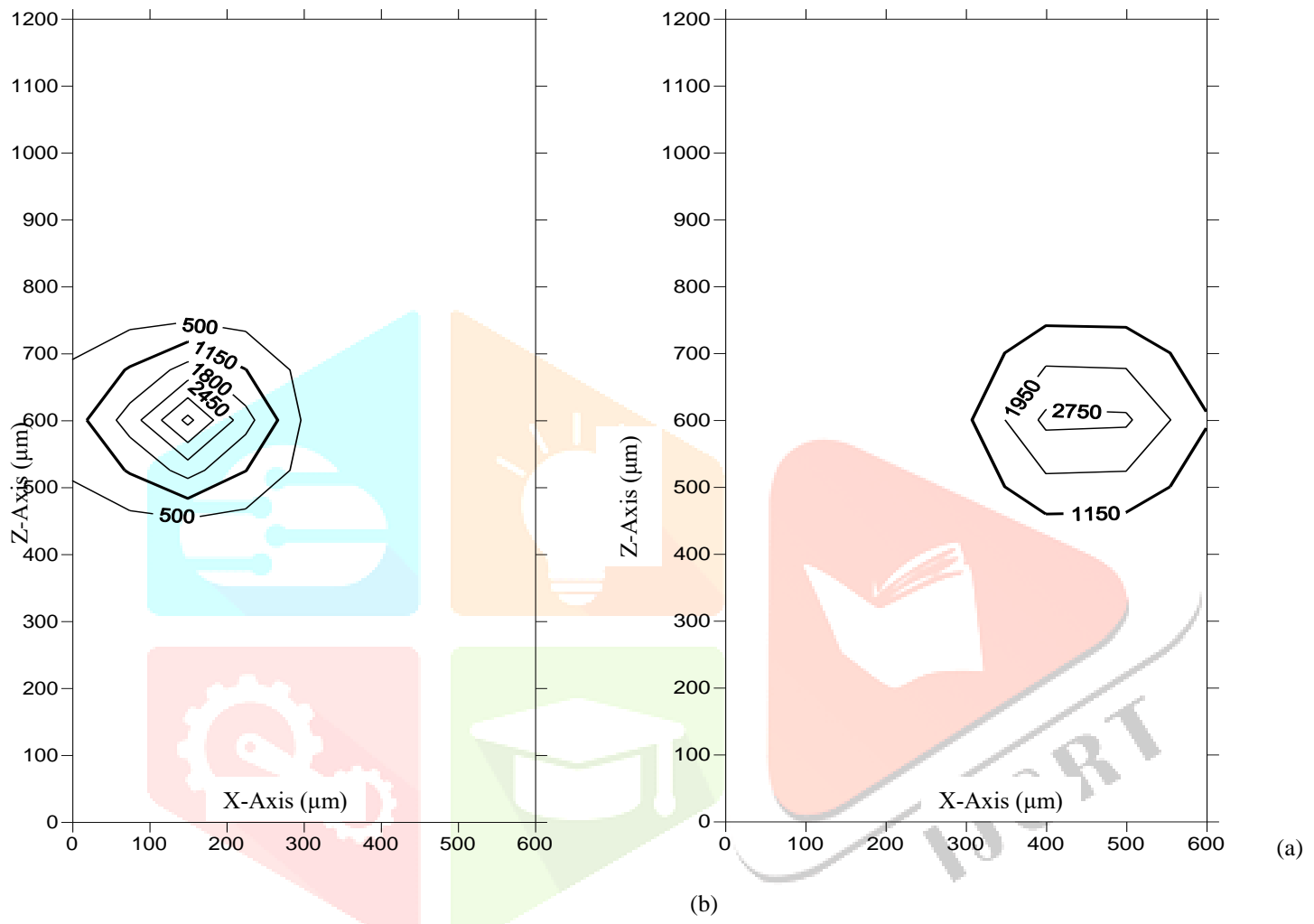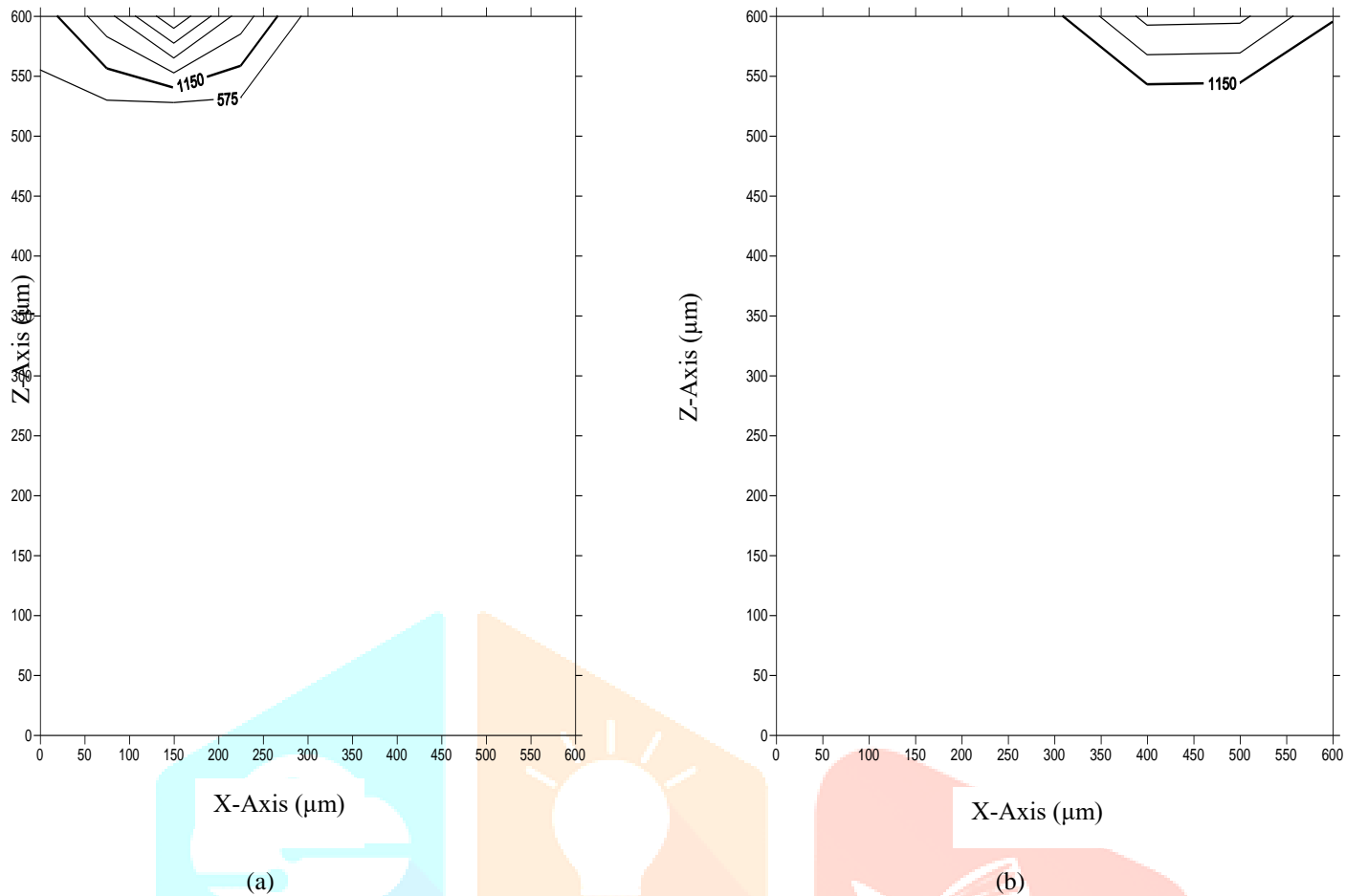
Fig. 6 Contour plots on X-Y plane at Z=0.6mm for 20V and 25A input power supply (a) after first spark at location X=0.15mm, Y=0.6mm (b) after second spark at location X=0.45mm, Y=0.6mm

Fig. 7 Variation of MRR with feed rate for different voltage

Fig.8 Schematic of BP neural network architecture

Fig. 9 Selection of number of neurons for 3 – N – 1 BP neural network architecture
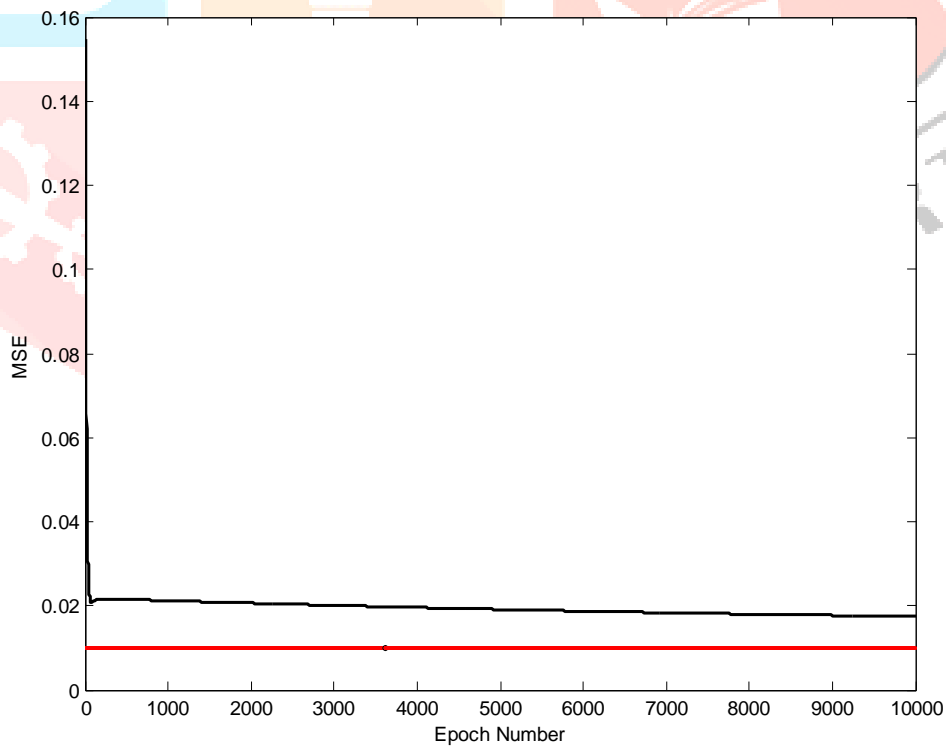
Fig. 10 Training of 3–7–1 BP neural network
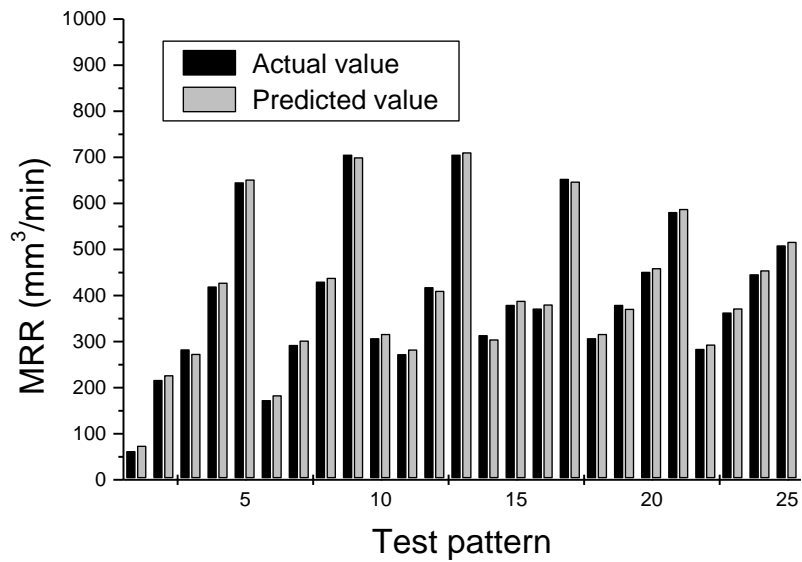
Fig. 11 Comparison between actual and predicted MRR
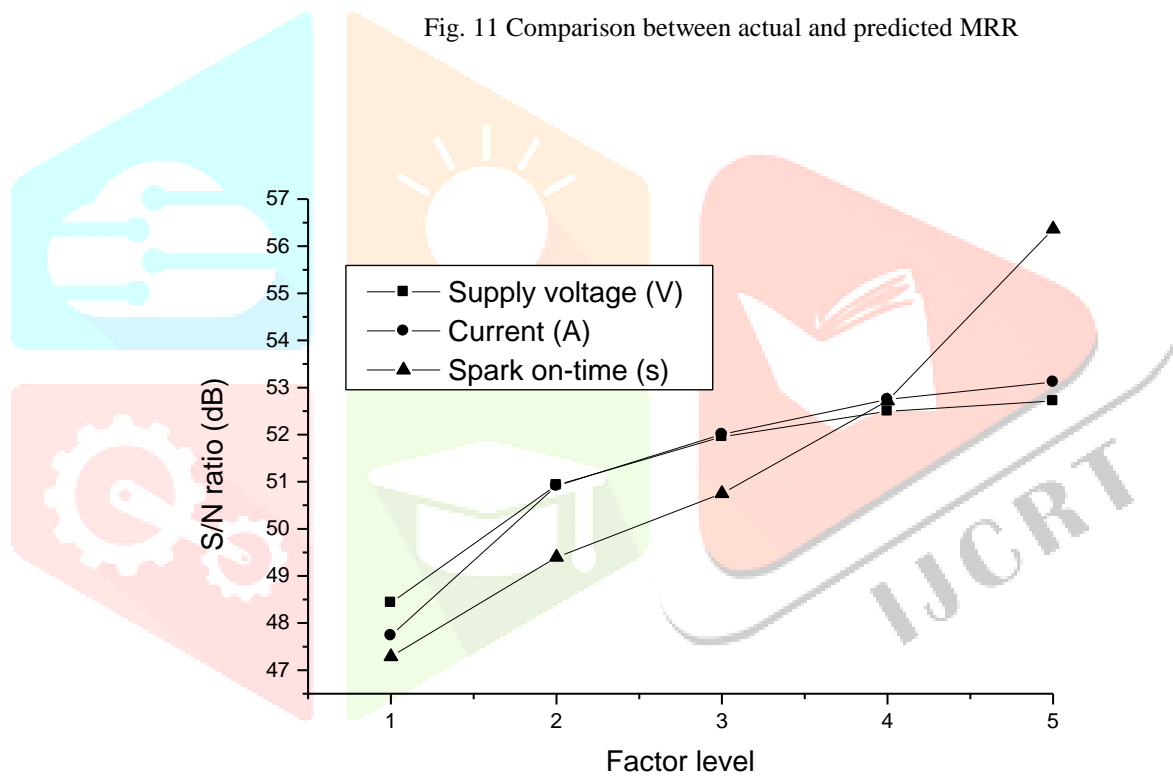
Fig.12 S/N based response graph for MRR

Table 1 Cutting Conditions

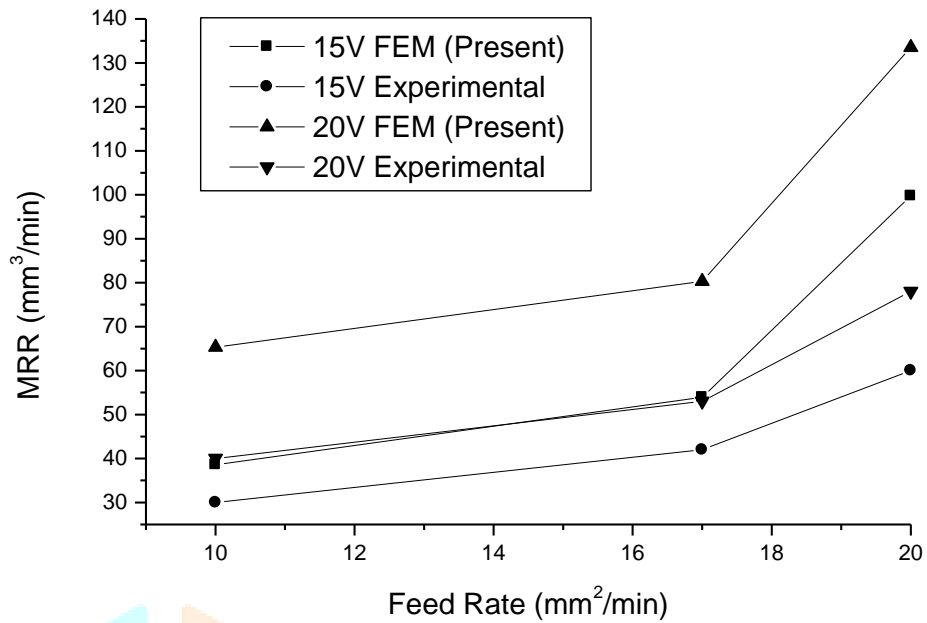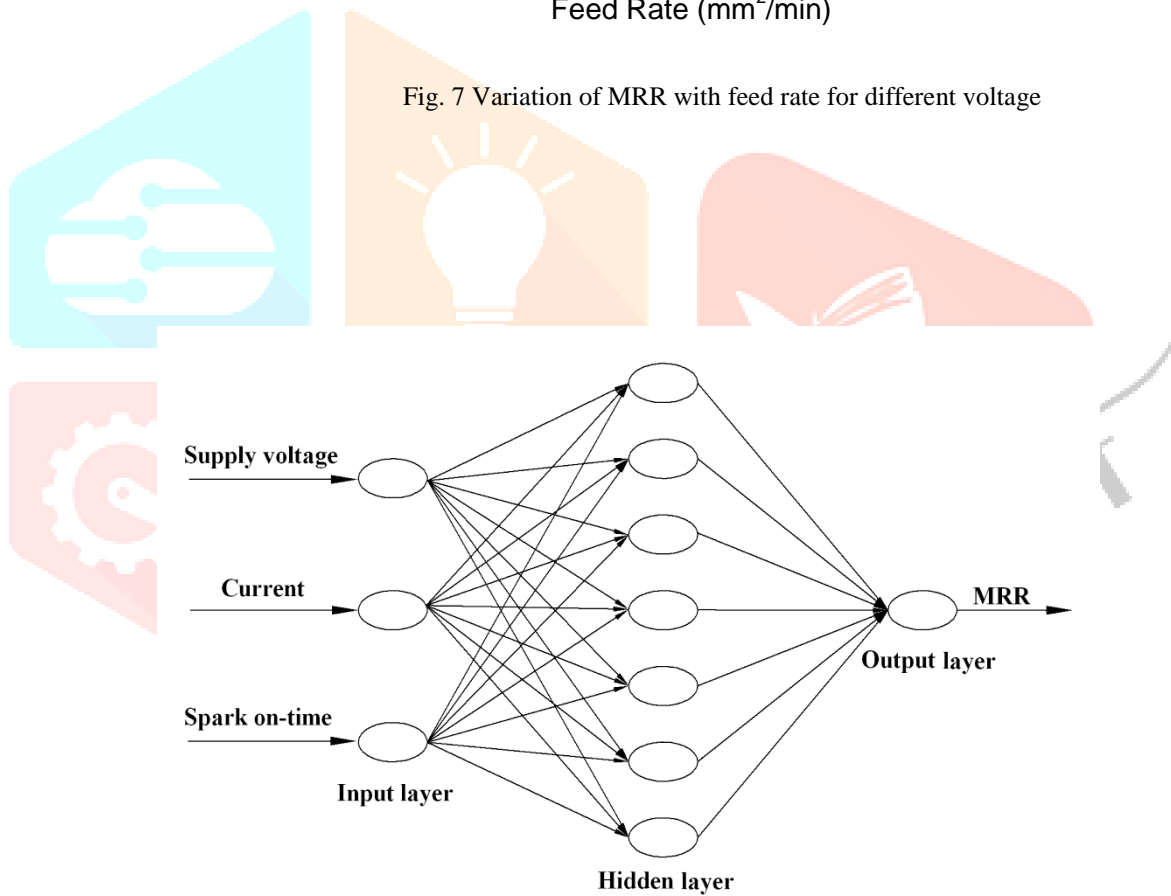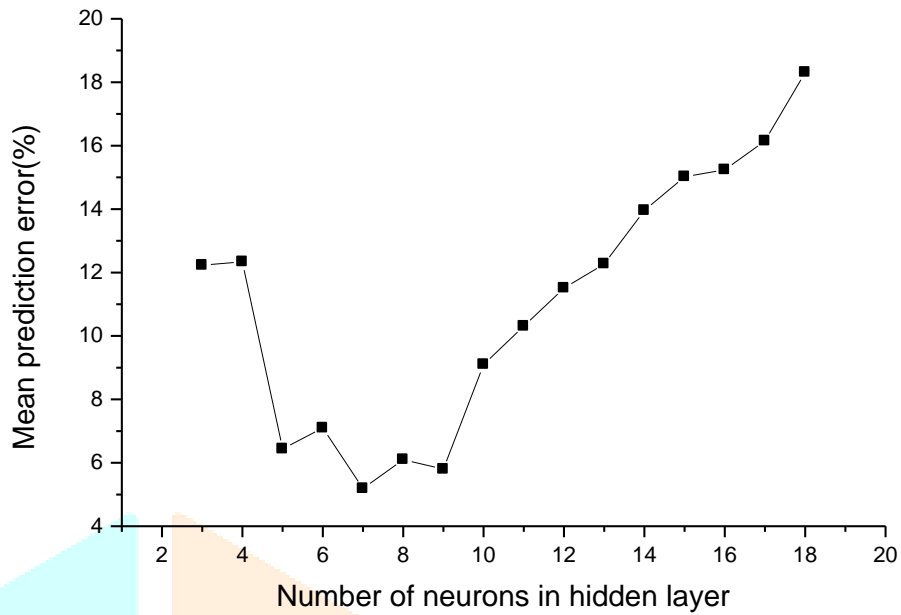|		
Electrolyte		NaNO$_3$
h (W/m^2-K)		20870
Supply voltage (V)		20
Current (A)		25
V$_w$ (m/min)		2
R (μm)		150
F$_w$	5 %	
t$_{on}$ (s)		0.0005
T$_0$ (K)		293

TABLE 2. **MATERIAL PROPERTIES OF MILD STEEL**

C$_p$ (J/Kg K)	461
k (W/m^2 K)	50.2
T$_m$ (^{0}C)	1150
ρ (kg/m^3)	7870

TABLE 3. **MATERIAL PROPERTIES OF GLASS**

C$_p$ (J/Kg K)	750
k (W/m^2 K)	1.14
T$_m$ (^{0}C)	820
ρ (kg/m^3)	2230

Table 4 Control factors and their levels used in the experiment

Symbol	Factors	Level 1	Level 2	Level 3	Level 4	Level 5
A	Supply Voltage (V)	20	30	40	50	60
B	Current (A)	10	20	30	40	50
C	Spark on-time (s)	0.0001	0.0003	0.0005	0.0007	0.0009

Table 5 ANN predicted response layout

	Factor level			MRR
Trials	A	B	C	(mm^3/min)
1	1	1	1	74.0095

2	1	2	2	227.0516
3	1	3	3	273.4264
4	1	4	4	427.8568
5	1	5	5	651.7632
6	2	1	2	183.5374
7	2	2	3	302.3529
8	2	3	4	438.3993
9	2	4	5	700.0421
10	2	5	1	316.6170
11	3	1	3	282.5894
12	3	2	4	409.7924
13	3	3	5	710.8922
14	3	4	1	304.6215
15	3	5	2	388.5076
16	4	1	4	380.6247
17	4	2	5	647.3416
18	4	3	1	316.6171
19	4	4	2	371.1457
20	4	5	3	459.2849
21	5	1	5	588.0237
22	5	2	1	293.7270
23	5	3	2	372.1608
24	5	4	3	454.1342
25	5	5	4	516.3277

Table 6 Testing of 3 – 7 – 1 BP neural network architecture

Factor level		Absolute prediction error (%)			
Trials	A	B	C		MRR
1	1	1	1		19.0789
2	1	2	2		4.7578
3	1	3	3		3.4085
4	1	4	4		1.9743
5	1	5	5		0.9326
6	2	1	2		6.2225
7	2	2	3		3.2621
8	2	3	4		1.9007
9	2	4	5		0.7690
10	2	5	1		3.0622
11	3	1	3		3.5739
12	3	2	4		1.9848
13	3	3	5		0.7690
14	3	4	1		2.9748

15	3	5	2		2.2855
16	4	1	4		2.3559
17	4	2	5		0.9102
18	4	3	1		3.0622
19	4	4	2		2.2855
20	4	5	3		1.7651
21	5	1		5	1.1466
22	5	2	1		3.3928
23	5	3	2		2.4349
24	5	4	3		1.7973
25	5	5	4		1.4520

Table 7 S/N ratios for MRR

Trials	S/N ratios (dB) MRR
1	37.3857
2	47.1225
3	48.7368
4	52.6259
5	56.2818
6	45.2745
7	49.6103
8	52.8374
9	56.9025
10	50.0105
11	49.0231
12	52.2513
13	57.0361
14	49.6752
15	51.7880
16	51.6099
17	56.2226
18	50.0107
19	51.3909
20	53.2416
21	55.3879
22	49.3588
23	51.4146
24	53.1437
25	54.2585

Table 8 Response table showing mean values of output at different level

Symbol	Factor	Level 1	Mean of raw data				
			Level 2		Level 3	Level 4	Level 5
A	Supply Voltage (V)		330.8215	388.1897	419.2806	435.0028	444.8747*
B	Current (A)		301.7569	376.0531	422.2992	451.5601	466.5001*
C	Spark on-time (s)		261.1184	308.4806	354.3576	434.6002	659.6126*

*Optimum level

Table 9 S/N response table showing mean values of MRR at different level

Symbol	Factor	Level 1	Mean S/N ratios (dB)				
			Level 2		Level 3	Level 4	Level 5
A	Supply Voltage		48.4305	50.9270	51.9547	52.4951	52.7127*
B	Current		47.7362	50.9131	52.0071	52.7476	53.1161*
C	Spark on-time	47.2882	49.3981	50.7511	52.7166	56.3662*

*Optimum level

Table 10 Results of raw data based ANOVA for MRR

Symbol	Factor	dof	Sum of squares	Mean squares	F	Contribution (%)
A	Supply Voltage	4	42348.998	10587.25	25.61	6.75
B	Current	4	88685.484	22171.37	53.64	14.13
C	Spark on-time	4	491384.893	122846.22	297.21	78.32
Error		12	4959.929	413.33		
Total		24	627379.304			100

Tabulated F-ratio at 95% confidence level: $F_{0.05, 4, 12}$ = 3.26

Table 11 Results of S/N based ANOVA for MRR

Symbol	Factor	dof	Sum of squares	Mean squares	F	Contribution (%)
A	Supply Voltage	4	61.1285	15.2821	6.14	14.45
B	Current	4	93.7202	23.4300	9.41	22.15
C	Spark on-time	4	238.4305	59.6076	23.95	56.35

Error	12	29.8671	2.4889		
Total	24	423.1463		100	

Tabulated F-ratio at 95% confidence level: $F_{0.05, 4, 12} = 3.26$

Table 12 Results of confirmation experiment

	Initial	Optimal
Factor level	$A_1 B_1 C_1$	$A_5 B_5 C_5$
MRR (mm^3/min)	74.0095	812.6244

References

1. Kurafuji, H. and Suda, K., "Electrical discharge drilling of glass," Annals of the CIRP, Vol. 16, pp. 415-419, 1968.
2. Wuthrich, R. and Fascio, V., "Machining of non-conducting materials using electrochemical discharge phenomenon-an overview," International Journal of Machine Tools and Manufacture, Vol. 45, pp. 1095-1108, 2005.
3. Basak, I. and Ghosh, A., "Mechanism of spark generation during electrochemical discharge machining: a theoretical model and experimental investigation," Journal of Materials Processing Technology, Vol. 62, pp. 46-53. 1996.
4. Jain, V. K., Dixit, P. M. and Pandey, P. M., "On the analysis of the electro chemical spark machining process," International Journal of Machine Tools and Manufacture, Vol. 39, pp. 165-186, 1999.
5. Kulkarni, A., Sharan, R. and Lal, G. K., "An experimental study of discharge mechanism in electrochemical discharge machining," International Journal of Machine Tools and Manufacture, Vol. 42, pp. 1121-1127, 2002.
6. Wuthrich, R. and Bleuler, H., "A model for electrode effects using percolation theory," Electrochimica Acta, Vol. 49, pp. 1547-1554, 2004.
7. Yerokhin, A. I., Nie, X., Leyland, A., Maetthews, A. and Dowey, S. J., "Plasma electrolysis for surface engineering," Surface and Coatings Technology, Vol. 122, pp. 73-93, 1999.
8. Vogt, H., "The anode effect as a fluid dynamic problem," Journal of applied Electrochemistry, Vol. 29, pp. 137-145, 1999.
9. Fascio, V., Wuthrich, R. and Bleuler, H., "Spark assisted chemical engraving in the light of electrochemistry," Electrochimica Acta, Vol. 49, pp. 3997-4003, 2004.
10. Wuthrich, R., Hof, L. A., Lal, A., Fujisaki, K., Bleuler, H., Mandin, Ph. and Picard, G., "Physical principles and miniaturization of spark assisted chemical engraving (SACE)," Journal of Micromechanics and Microengineering, Vol. 15, pp. 268-275, 2005.
11. McGeough, J. A. and Hofy, H. El., "Evaluation of an Apparatus for Electrochemical Arc Wire-Machining," Journal of Engineering for Industry, Vol. 110, pp. 119-123, 1988.
12. Jain, V. K., Rao, P. S., Choudhury, S. K. and Rajurkar, K. P., "Experimental investigations into traveling wire electrochemical spark machining (TW-ECSM) of composites," Transactions of ASME, Journal of Engineering for Industry, Vol. 113, pp. 75-84, 1991.
13. Peng, W. Y. and Liao, Y. S., "Study of electrochemical discharge machining technology for slicing non-conductive brittle materials," Journal of Materials Processing Technology, Vol. 149, pp. 363-369, 2004.
14. Nesarikar, V. V., Jain, V. K. and Choudhury, S. K., "Traveling wire electrochemical spark machining of thick sheets of Kevlar-Epoxy composites," Proceedings of the Sixteenth AIMTDR Conference, pp. 672-677, 1994.
15. Singh, Y. P., Jain, V. K., Kumar, P. and Agrawal, D. C., "Machining piezoelectric (PZT) ceramics using an electrochemical spark machining (ECSM) process," Journal of Materials Processing Technology, Vol. 58, pp. 24-31, 1996.
16. Basak, I. and Ghosh, A., "Mechanism of material removal in electrochemical discharge machining: a theoretical model and experimental verification," Journal of Materials Processing Technology, Vol. 71, pp. 350- 359, 1997.
17. Bhondwe, K. L., Yadava, V. and Kathiresan, G., "Finite element prediction of material removal rate due to electrochemical spark machining," International Journal of Machine Tools and Manufacture, Vol. 46, pp. 1699-1706, 2006.
18. Panda, M. C. and Yadava, V., "Finite element prediction of material removal rate due to traveling wire electrochemical spark machining," International Journal of Advanced Manufacturing Technology, doi: 10.1007/s00170-009-1992-0, 2009.
19. Cengel, Y. A., Heat Transfer a Practical Approach, 2nd ed. Tata McGraw-Hill Publishing Company Limited, New Delhi, 2004.
20. Reddy, J.N., An Introduction to Finite Element Method, 3rd ed. Tata McGraw-Hill Publishing Company Limited, New Delhi, 2005.
21. Nayar, A., The steel hand book, Tata McGraw-Hill Publishing Company Limited, New Delhi, 2002.
22. Hassoun, M. H., Fundamentals of Artificial Neural Networks, Prentice–Hall of India Private Limited, New Delhi, 2007.
23. Zurada, J. M., Introduction to Artificial Neural Systems, 10th ed., Jaico publishing house, Mumbai, 2006.
24. Karunakar, D. B. and Datta, G. L., "Prevention of defects in castings using back propagation neural networks," International Journal of Advanced Manufacturing Technology, Vol. 39, pp. 1111-1124, 2008.

25. Jain, R. K. and Jain, V. K., "Optimum selection of machining conditions in abrasive flow machining using neural network," Journal of Materials Processing Technology, Vol. 108, pp. 62-67, 2000.
26. Fausett, L., Fundamentals of neural networks: architectures, algorithms and applications, Prentice-Hall, New York, 1994.
27. Phadke, M. S., Quality Engineering using Robust Design, Prentice-Hall, Englewood Cliffs, 1989.
28. Ross, P. J., Taguchi Techniques for Quality Engineering, 2nd ed., Tata McGraw-Hill Publishing Company Limited, New Delhi, 2005.